

## GAFD Special issue on “Physics and Algorithms of the Pencil Code”

### *The time step constraint in radiation hydrodynamics\**

AXEL BRANDENBURG<sup>a,b,c,d†</sup> and UPASANA DAS<sup>a,b</sup>

<sup>a</sup>JILA, Box 440, University of Colorado, Boulder, CO 80303, USA

<sup>b</sup>Nordita, KTH Royal Institute of Technology and Stockholm University,  
 Roslagstullsbacken 23, SE-10691 Stockholm, Sweden

<sup>c</sup>Laboratory for Atmospheric and Space Physics, University of Colorado, Boulder, CO 80303, USA

<sup>d</sup>Department of Astronomy, Stockholm University, SE-10691 Stockholm, Sweden

(December 15, 2024, Revision: 1.101)

Explicit radiation hydrodynamic simulations of the atmospheres of massive stars and of convection in accretion discs around white dwarfs suffer from prohibitively short time steps due to radiation. This constraint is related to the cooling time rather than the radiative pressure. We show that the radiative time step constraint is governed by the minimum of the sum of the optically thick and thin contributions rather than the smaller of the two. In simulations with the PENCIL CODE, their weighting fractions are found to be about 0.2 and 4.2, respectively. In three-dimensional convective accretion disk simulations, the Deardorff term is found to be the main contributor to the enthalpy flux. We conclude with a discussion of how to mitigate the radiative time step problem.

**Keywords:** Numerical stability; Radiative cooling; Convection; Accretion discs; Hot stars

### 1. Introduction

Numerical simulations have long played an essential role in facilitating our understanding of hydrodynamic processes in astrophysics. The cost of such simulations is determined not only by the numerical mesh resolution, but also by the length of the time step. In hydrodynamics, the maximum permissible time step decreases linearly with increasing spatial mesh resolution in such a way that the information that is passed from one time step to the next cannot propagate by more than roughly one mesh spacing  $\delta x$ . The length of the time step  $\delta t$  is therefore of the order of  $\delta x/c$ , where  $c$  is the speed of the fastest propagating mode (for example the speed of sound). This is known as the Courant-Friedrichs-Lewy (CFL) condition (Courant et al. 1928) in ordinary hydrodynamics. This condition changes for diffusive processes with diffusivity  $\chi$ , where the time it takes to propagate information from one mesh point to the next is of the order of  $\delta x^2/\chi$  (e.g. Caunt & Korpi 2001). Thus, decreasing the mesh width by a factor of two implies a reduction of the time step by a factor of four.

In the deeper layers of a star, the opacity (per unit volume) is large and the mean free path is small, so the optically thick approximation is applicable. As one approaches the outer layers, however, the opacity decreases sharply and the mean free path becomes long compared to other typical scales in the system. If one were to continue using the optically thick approximation, the diffusivity would become larger and larger. This would have severe consequences for the length of the time step. In reality, however, the optically thick approximation becomes invalid

---

\*Dedicated to Professor Ed A. Spiegel

†Email: brandenb@nordita.org

and no stringent time step constraint is expected to occur in the optically thin regime – at least not for solar-type stars. Nevertheless, for hotter stars there can be layers in the proximity of the photosphere when the time step constraint can become rather stringent.

In the present paper, we will be concerned with radiation transport using what is nowadays often called long characteristics (Mihalas 1978, Nordlund 1982). In this case there is no time advancement and the radiation field is propagated instantaneously across all rays without imposing any direct time step constraint. However, radiation interacts with the velocity field through radiation pressure and the temperature field through heating and cooling processes. While neither of these processes usually impose computationally prohibitive time step constraints in solar physics (Stein & Nordlund 1989, 1998), a serious time step constraint (more stringent than the hydrodynamic time step) has been encountered empirically in numerical solutions of hot atmospheres (Spiegel 2006) where radiation pressure contributes to the hydrostatic equilibrium (Brandenburg & Spiegel 2006, unpublished). One possibility is that the radiative pressure was responsible for this short time step constraint. More recently (Brandenburg & Das 2018, again unpublished), we have encountered a similar time step constraint when solving the radiation hydrodynamics equations for hot accretion discs around white dwarfs. Similar calculations have been carried out by Coleman et al. (2018) using the ZEUS code (Stone & Norman 1992a,b, Stone et al. 1992). However, since we did not include radiation pressure in those solutions, the radiation pressure could not be held responsible here. This motivates a more detailed study of the time step constraints in explicit radiation hydrodynamics using long characteristics. We do not consider here implicit solvers, which could avoid those problems, but are computationally more costly. Our hope is that by diagnosing in more detail the radiative time step constraints in different situations, we would be in a better position to mitigate the problem of short time steps. One possibility might be to adopt certain changes in the physical setup, while still being able to capture the essential physics. This will be discussed at the end of this paper.

## 2. Radiative cooling constraint

To quantify the expected time step constraint in radiation hydrodynamics, we begin by computing the cooling time. We have to consider the radiation transport equation for the intensity  $I(\mathbf{x}, t, \hat{\mathbf{n}})$ , where  $\mathbf{x}$  is position,  $t$  is time, and  $\hat{\mathbf{n}}$  is the direction of the ray. In the grey approximation, it is

$$\hat{\mathbf{n}} \cdot \nabla I = -\kappa\rho(I - S), \tag{1}$$

where  $\rho$  is the density,  $\kappa$  is the opacity, and  $S(\mathbf{x}, t)$  is the source function, which we will assume to be given by the Planck function, i.e.,  $S = (\sigma_{\text{SB}}/\pi)T^4$ , with  $\sigma_{\text{SB}}$  being the Stefan-Boltzmann constant and  $T$  the temperature.

To gain insight into the nature of radiation in the optically thin and thick cases, it is useful to adopt a model where we can assume constant coefficients, which allows us to use Fourier transformation. We also adopt the Eddington approximation, where the moment expansion is closed by assuming the radiation pressure to be isotropic and given by  $\frac{1}{3}\delta_{ij}J$ , where  $J = \int_{4\pi} I d\Omega/4\pi$  is the mean intensity and  $d\Omega$  is the differential over the solid angle. This yields (Edwards 1990)

$$\frac{1}{3}(\ell\nabla)^2 J = J - S, \tag{2}$$

where  $\ell = (\kappa\rho)^{-1}$  is the photon mean-free path. In the absence of any heating and cooling processes other than the negative radiative flux divergence ( $-\nabla \cdot \mathbf{F}_{\text{rad}}$ ), which is proportional

to  $(\ell \nabla)^2 J$ , the temperature evolution is governed by the equation

$$\rho c_p \frac{DT}{Dt} - \frac{Dp}{Dt} = 4\pi\kappa\rho (\ell \nabla)^2 J, \quad (3)$$

which is valid both in the optically thick and thin cases. Here,  $p$  is the pressure,  $c_p$  is the specific heat at constant pressure and  $D/Dt = \partial/\partial t + \mathbf{u} \cdot \nabla$  is the advective derivative. For the purpose of the present discussion, we assume  $p = \text{const}$  and omit the  $Dp/Dt$  term. Linearising equation (3) about a hydrostatic homogeneous equilibrium solution with  $\mathbf{u} = \mathbf{0}$ ,  $T = \text{const}$ , and  $\rho = \text{const}$ , and assuming the solution to be proportional to  $e^{ikz - \lambda t}$ , we find for the cooling or decay rate  $\lambda$  the expression (Spiegel 1957, Unno & Spiegel 1966)

$$\lambda = \frac{c_\gamma \ell k^2 / 3}{1 + \ell^2 k^2 / 3} = \frac{\chi k^2}{1 + \ell^2 k^2 / 3}, \quad (4)$$

where  $k$  is the wavenumber. Note that we have defined the quantity  $c_\gamma = 16\sigma_{\text{SB}}T^3/\rho c_p$ , which plays the role of a characteristic velocity of photon diffusion (Barekat & Brandenburg 2014), and  $\chi = c_\gamma \ell / 3$  is the radiative diffusivity.

When  $\ell$  is small in the sense that  $k\ell \ll 1$ , the cooling rate is  $\lambda \approx \chi k^2 = c_\gamma \ell k^2 / 3$ , which corresponds to the usual expression in the optically thick limit. On the other hand, in the optically thin limit,  $\ell \rightarrow \infty$ , we have  $\lambda \approx c_\gamma / \ell$ , so cooling becomes independent of  $k$ . The resulting value of  $\lambda$  is much smaller than the value of  $c_\gamma \ell k^2 / 3$ , which it would be if one continued using the expression for the optically thick case even though  $k\ell \gg 1$ . Thus, when using the correct expression, it may seem that radiation is less likely to be a limiting factor in the time step consideration. However, as we will show in this work, this is not necessarily true.

To arrive at an expression for the time step constraint due to radiation, we express the cooling time as the inverse of the cooling rate,  $\tau_{\text{cool}} = \lambda^{-1}$ , i.e.,

$$\tau_{\text{cool}} = \frac{1}{\chi k^2} + \frac{\ell}{c_\gamma}. \quad (5)$$

The first and second terms on the right-hand side of equation (5) characterise the contributions from the optically thick and thin parts, respectively, and  $k$  should be replaced by the Nyquist wavenumber,  $k_{\text{Ny}} = \pi/\delta z$ . Here, and in the following sections, we restrict our attention to the vertical mesh spacing  $\delta z$ . In general, the direction with the finest mesh spacing will impose the strongest constraint.

The parts for the optically thick and thin regions may contribute with different non-dimensional prefactors to the actual (empirically determined) time step constraint. Nevertheless, we will assume that the time step limit will still depend on the sum of these two parts, just like in equation (5), because that ensures that in the optically thin regime, the much faster cooling rate relevant for the optically thick limit does not contribute. For a global simulation to be stable in both regimes, the time step can therefore not exceed the shortest value of the sum anywhere in the domain. Keeping this in mind, we define the radiative time step to be

$$\delta t_{\text{rad}} = C_{\text{rad}}^{\text{thick}} \frac{\delta z^2}{\chi} + C_{\text{rad}}^{\text{thin}} \frac{\ell}{c_\gamma}, \quad (6)$$

such that the corresponding maximum permissible time step is given by

$$\delta t \leq \min(\delta t_{\text{rad}}), \quad (7)$$

where  $C_{\text{rad}}^{\text{thick}}$  and  $C_{\text{rad}}^{\text{thin}}$  are dimensionless coefficients that we will estimate numerically in this work.

It is useful to reflect again on the somewhat unusual form of equation (7) as a time step constraint, because the usual CFL condition is formulated in terms of the shortest one of

several constraints, e.g.,  $\delta t = \min(\delta z/c_s, \delta z^2/\chi)$ , where  $c_s$  is the sound speed. Alternatively, one could express the inverse time step as the sum of the inverse of the contributions, i.e.,  $\delta t^{-1} = \max(c_s/\delta z + \chi/\delta z^2)$ . In equation (7), by contrast,  $\delta t_{\text{rad}}$  itself is determined as a sum of time steps. In full radiation hydrodynamics, the maximum permissible time step will therefore be the minimum of  $\delta t_{\text{rad}}$ , as given by equation (6), and the usual CFL and viscous constraints, i.e.,

$$\delta t = \min \left( C_{\text{rad}}^{\text{thick}} \frac{\delta z^2}{\chi} + C_{\text{rad}}^{\text{thin}} \frac{\ell}{c_\gamma}, C_{\text{CFL}} \frac{\delta z}{c_s}, C_{\text{visc}} \frac{\delta z^2}{\nu D} \right). \quad (8)$$

For the PENCIL CODE with its default third order time stepping scheme,  $C_{\text{CFL}} = 0.9$  is the usual CFL number,  $C_{\text{visc}} = 0.25$  is the viscous time step constraint, with  $\nu$  being the kinematic viscosity and  $D$  the dimensionality. In our present one-dimensional calculation, we have  $D = 1$ . In three dimensions,  $C_{\text{visc}}/D = 0.08$  is in fact slightly larger than the value of 0.05 quoted by Caunt & Korpi (2001). The reason  $D$  enters is because the discretised form of the second derivative, relevant in the optically thick formulation, has a larger coefficient at the center point where the derivative is evaluated.<sup>1</sup> In the simulations reported below, we have tested that the  $D$  factor does not enter in the treatment of radiation with long characteristics.

We emphasise that there is no analogy in how the optically thick and thin contributions enter into the time step constraint and how the usual CFL and viscous constraints enter. This becomes strikingly clear by stating

$$\delta t \neq \min \left( C_{\text{rad}}^{\text{thick}} \frac{\delta z^2}{\chi}, C_{\text{rad}}^{\text{thin}} \frac{\ell}{c_\gamma}, C_{\text{CFL}} \frac{\delta z}{c_s}, C_{\text{visc}} \frac{\delta z^2}{\nu D} \right). \quad (9)$$

Later in this paper, we will see examples where either  $\delta z^2/\chi$  or  $\ell/c_\gamma$  may be very small, and yet, neither of those affect the time step if the other term is large.

The goal of the present paper is to test the validity of equation (7) in the case when radiation is treated with long characteristics. We also compare with the usual CFL condition, where the time step is constrained by  $\delta t_s = C_{\text{CFL}} \delta z/c_s$ . Since the role of  $c_\gamma$  is not entirely clear, especially when radiation pressure also enters the problem, we ask whether a similarly defined quantity  $\delta t_\gamma = C_\gamma \delta z/c_\gamma$  might constrain the time step further, even though it does not explicitly feature in equation 8. Our numerical experiments reported below show that  $\delta t_\gamma$  itself does not constrain the time step, but the ratio  $c_s/c_\gamma$  may play an important role; see discussion in section 5. Note that  $C_\gamma$  is expected to be of the order of unity as  $t_\gamma \propto \delta z$  and, hence, we use  $C_\gamma = C_{\text{CFL}} = 0.9$  in our plots below. Regarding the value of  $C_{\text{rad}}^{\text{thick}}$ , we expect it to be comparable to  $C_{\text{visc}}$ , but our experiments reported below seem to be consistent with a slightly smaller value of  $C_{\text{rad}}^{\text{thick}} = 0.2$ , so we will use that value in all the corresponding plots shown below. Finally, regarding the value of  $C_{\text{rad}}^{\text{thin}}$ , it is important to note that it enters without a  $\delta z$  term; see second term in equation 7. Therefore, in order to obtain a preliminary estimate, we can empirically test the radiative time step constraint in the optically thin case by using a zero-dimensional model (i.e., with one mesh point). In this way, we find that  $C_{\text{rad}}^{\text{thin}} \approx 4.2$  and we use this value in the plots shown below. We find that the values of the various coefficients quoted here are consistent with the empirically determined ones, as discussed in detail in section 4.3 and table 2.

In this paper, we discuss two distinct models where severe time step constraints have been encountered. One is the model of Spiegel (2006) and the other is a local model of an accretion disc, similar to that of Coleman et al. (2018). Radiation pressure is included in the former,

<sup>1</sup>For a second order discretisation, for example, we have  $\nabla^2 f_i = (f_{i+1} - 2f_i + f_{i-1})/\delta x^2$  in one dimension, but  $\nabla^2 f_{ij} = (f_{i+1j} + f_{ij+1} - 4f_{ij} + f_{i-1j} + f_{ij-1})/\delta x^2$  in two dimensions, so at the center point,  $f_{ij}$ , the coefficient increases from  $2/\delta x^2$  to  $4/\delta x^2$  in two dimensions, and to  $6/\delta x^2$  in three dimensions. This applies analogously also to the sixth order discretisation used in the PENCIL CODE.

but not in the latter. It will turn out that the time step constraints are quite different from each other in the two cases, although this difference is not explicitly linked to the presence or absence of radiation pressure.

### 3. Our models

#### 3.1. The basic equations

We consider here the equations solved by default in the PENCIL CODE. The basic dependent variables are the logarithmic density  $\ln \rho$ , the velocity  $\mathbf{u}$ , and the specific entropy  $s$ , which obey the equations

$$\frac{D \ln \rho}{Dt} = -\nabla \cdot \mathbf{u}, \quad (10)$$

$$\rho \frac{D\mathbf{u}}{Dt} = -\nabla p + \rho \mathbf{g} + \frac{\rho \kappa}{c} \mathbf{F}_{\text{rad}} + \nabla \cdot \boldsymbol{\tau}, \quad (11)$$

$$\rho T \frac{Ds}{Dt} = \mathcal{H} - \nabla \cdot \mathbf{F}_{\text{rad}} + \boldsymbol{\tau} : \nabla \mathbf{U}, \quad (12)$$

$$\hat{\mathbf{n}} \cdot \nabla I = -\kappa \rho (I - S), \quad \mathbf{F}_{\text{rad}} = \int_{4\pi} \hat{\mathbf{n}} I d\Omega, \quad \nabla \cdot \mathbf{F}_{\text{rad}} = \int_{4\pi} (I - S) d\Omega, \quad (13)$$

where  $\mathbf{g} = (0, 0, -g)$  is the gravitational acceleration in Cartesian coordinates  $(x, y, z)$ ,  $c$  is the speed of light,  $\mathbf{F}_{\text{rad}}$  is the radiative flux,  $\boldsymbol{\tau} = 2\rho\nu\mathbf{S}$  is the stress tensor if there is just shear viscosity,  $S_{ij} = \frac{1}{2}(\partial_i u_j + \partial_j u_i) - \frac{1}{3}\delta_{ij}\nabla \cdot \mathbf{u}$  are the components of the traceless rate-of-strain tensor,  $\mathcal{H}$  is a heating function to be specified below,  $\boldsymbol{\tau} : \nabla \mathbf{U} = \tau_{ij}\partial u_i/\partial x_j$  is the viscous heating term, and equation (1) has been restated in equation (13) for completeness. In the model for the upper layers of a star, we have  $g_z = \text{const} < 0$ , while in our accretion disc model with local Keplerian angular velocity  $\Omega$ ,  $g_z = -\Omega^2 z$  increases linearly with the distance  $z$  from the midplane.

The equations of radiation transport (13) have been implemented into the PENCIL CODE by Heinemann et al. (2006), and were then used in the solar context (Heinemann et al. 2007) and also for more idealised problems (Barekat & Brandenburg 2014). In the outer layers of the Sun, partial ionisation is also important, so one needs to solve the Saha equation, for which temperature needs to be known. It is then advantageous to use  $\ln T$  as the dependent variable instead of  $s$ . Again, this implementation into the PENCIL CODE goes back to the work of (Heinemann et al. 2007), and more idealised models with ionisation and radiation have been considered by Bhat & Brandenburg (2016).

In the presence of shocks, it is often useful to increase the viscosity locally in those regions where the velocity converges, i.e., where the flow divergence is negative or  $\nabla \cdot \mathbf{u} < 0$ . This approach goes back to von Neumann & Richtmyer (1950). In practice, one defines the shock viscosity as

$$\nu_{\text{shock}} = C_{\text{shock}} \delta x^2 \langle -\nabla \cdot \mathbf{u} \rangle_+, \quad (14)$$

where  $\langle \dots \rangle_+$  denotes a running five point average over all positive arguments,  $C_{\text{shock}}$  is the coefficient of the shock viscosity, and  $\delta x = \delta y = \delta z$  are the mesh spacings in all three directions. This shock viscosity is applied as a bulk viscosity, i.e., we have

$$\tau_{ij} = 2\rho\nu S_{ij} + \rho\nu_{\text{shock}} \delta_{ij} \nabla \cdot \mathbf{u}. \quad (15)$$

At the end of this paper, we present one case where a shock viscosity is applied and show how it affects the time step; see section 4.4 and figures 8 and 9.

### 3.2. Stratification of hot stellar surface layers

In hot stellar surface layers, the radiation pressure plays an important role. This is typically also the regime in which the electron scattering opacity is important (Frank et al. 1992), i.e.,

$$\kappa = \kappa_{\text{es}} \approx 0.34 \text{ cm}^2 \text{ g}^{-1}. \quad (16)$$

Since this is a constant, and since the radiative flux  $F_{\text{rad}}$  is also constant in radiative equilibrium, we just have to replace gravity by the effective one, which is then still a constant, i.e.,

$$g \rightarrow g_{\text{eff}} = g - (\kappa/c) F_{\text{rad}} = \text{const}. \quad (17)$$

We integrate the equations of hydrostatic and radiative equilibrium,

$$\frac{dp}{dz} = -\rho g_{\text{eff}}, \quad \frac{dT}{dz} = -\frac{F_{\text{rad}}}{K}, \quad (18)$$

with  $F_{\text{rad}} = \sigma_{\text{SB}} T_{\text{eff}}^4 = \text{const}$ , where  $T_{\text{eff}}$  is the effective temperature of the stellar surface and  $K = \rho c_p \chi$ . Note that the equation for  $dT/dz$  applies even in the optically thin case provided the system is in thermal equilibrium. This is because in equilibrium we have  $\nabla \cdot \mathbf{F}_{\text{rad}} = 0$ , and therefore  $J = S$ , just like in the optically thick case. In the time-dependent case, however, as discussed above, the optically thick and thin cases are quite different from each other.

Next, it is convenient to divide the two equations in (18) by each other, so we obtain,

$$\frac{dT}{dp} = \frac{F_{\text{rad}}}{K \rho g_{\text{eff}}}. \quad (19)$$

In astrophysics, the symbol  $\nabla$  is used to denote the double-logarithmic temperature gradient, so  $\nabla = d \ln T / d \ln p$ , and for the present radiative equilibrium solution, the radiative temperature gradient is denoted by  $\nabla_{\text{rad}}$ . Thus, we have

$$\nabla_{\text{rad}} \equiv \frac{d \ln T}{d \ln p} = \frac{p F_{\text{rad}}}{K T \rho g_{\text{eff}}} = \frac{(c_p - c_v) F_{\text{rad}}}{K g_{\text{eff}}}, \quad (20)$$

where we have used  $p = (c_p - c_v) T \rho$  for the equation of state of a perfect gas and  $c_v$  is the specific heat at constant volume.

The vertical specific entropy gradient is  $d(s/c_p)/d \ln p = \nabla - \nabla_{\text{ad}}$ , so the Schwarzschild criterion for convective stability (positive outward gradient of  $s$ ) is  $\nabla < \nabla_{\text{ad}}$ . Convection occurs when  $\nabla > \nabla_{\text{ad}}$ . This mixes the fluid, so  $s$  becomes uniform and one must replace  $\nabla$  by  $\nabla_{\text{ad}} = 1 - 1/\gamma = 0.4$ , which is the value for a monatomic gas with  $\gamma = c_p/c_v = 5/3$ . Thus, the local double-logarithmic temperature gradient can be written as (see, e.g., Kähler 1972)

$$\nabla = \min(\nabla_{\text{ad}}, \nabla_{\text{rad}}). \quad (21)$$

In more realistic mixing length descriptions of stellar convection, this relation is to be replaced by a smooth transition between the two states; see Vitense (1953) for the original formulation, which corresponds to finding a solution to the equation

$$(\nabla - \nabla_{\text{rad}}) + \epsilon_* (\nabla - \nabla_{\text{rad}})^\xi \quad (\text{for } \nabla_{\text{rad}} > \nabla_{\text{ad}}) \quad (22)$$

with  $\xi = 3/2$ ,  $\epsilon_* = \iota c_s^3 / \chi g$ , and  $\iota$  being a coefficient of the order of unity; see figure 3 of Brandenburg (2016) for a comparison of solutions for  $\xi = 3/2$  and  $\xi = 1$ .

For lower temperatures, the opacity given by equation (16) is no longer valid. A more general representation is given in terms of combinations of Kramers-type opacities

$$\frac{1}{\kappa} = \frac{1}{\kappa_{\text{H}^-}} + \frac{1}{\kappa_{\text{Kr}} + \kappa_{\text{es}}}, \quad (23)$$

where we use,

$$\kappa_i = \kappa_0 (\rho/\rho_0)^{a_i} (T/T_0)^{b_i}, \quad (24)$$

where  $i = \text{Kr}, \text{H}^-$ ; with  $\kappa_0 = 10^4 \text{ cm}^2 \text{ g}^{-1}$ ,  $\rho_0 = 10^{-5} \text{ g cm}^{-3}$ ,  $T_0 = 13,000 \text{ K}$ , and  $a_{\text{Kr}} = 1$ ,  $b_{\text{Kr}} = -3.5$  for the Kramers opacity  $\kappa_{\text{Kr}}$  relevant for deeper layers in the solar convection zone, and  $a_{\text{H}^-} = 0.5$ ,  $b_{\text{H}^-} = 18$  for the  $\text{H}^-$  opacity  $\kappa_{\text{H}^-}$  in the layers just beneath the solar photosphere. These were also the coefficients used by Brandenburg (2016). The same opacity prescription will also be used in our accretion disc models described below.

To obtain a solution, we assume  $T_{\text{eff}}$  and  $g_{\text{eff}}$  as given. For grey atmospheres, the temperature of the atmosphere far above the photosphere is  $T_0 = T_{\text{eff}}/2^{1/4} \approx 0.84 T_{\text{eff}}$ ; see Stix (2002) for a recent text book on this. Thus, we integrate from the top downward using  $\ln p$  as the independent variable starting with a sufficiently low value. For single power law opacities, such as a simple Kramers-type opacity with fixed exponents  $a$  and  $b$ , this integration can be done analytically (see appendix A of Brandenburg 2016), but here we use more complicated opacities and do the integration numerically. At each height, we solve equation (22) for  $\nabla$  to determine the temperature gradient when  $\nabla_{\text{rad}} > \nabla_{\text{ad}}$ .

### 3.3. Accretion disc model

Accretion discs are generally heated by turbulent dissipation. To model this realistically, we would need to simulate accretion disc turbulence through a combination of (i) the magneto-rotational instability (MRI) to generate turbulence from a given magnetic field (Balbus & Hawley 1991) and (ii) the dynamo instability to regenerate the required magnetic field (Brandenburg et al. 1995). To simplify matters, and to avoid modelling the MRI and the dynamo, we assume instead a prescribed heating function as a function of  $z$ ,

$$\mathcal{H}(z) = \left(\frac{3}{2}\Omega\right)^2 \frac{\dot{M}}{3\pi} \frac{\Theta(z_{\text{heat}} - |z|)}{z_{\text{heat}}}, \quad (25)$$

where we have used the usual parameterisation for accretion discs in terms of mass accretion rate  $\dot{M}$  and local Keplerian angular velocity  $\Omega$  (Frank et al. 1992). In addition, we have assumed a vertical profile  $\Theta(z_{\text{heat}} - |z|)$ , which is unity inside the disc,  $|z| \leq z_{\text{heat}}$ , and zero outside. In practice, we initiate our simulations by using an isothermal hydrostatic stratification, where  $g = \Omega^2 z$  is the vertical gravity and  $\ln(\rho/\rho_0) = -z^2/2H_p^2$ , with  $H_p = c_s/\Omega$  being the pressure scale height,  $c_s = \sqrt{\mathcal{R}T/\mu}$  the isothermal sound speed,  $\mathcal{R}$  the universal gas constant,  $\rho_0$  the density at  $z = 0$ , and  $\mu$  the mean atomic weight. Radiation then causes the outer layers to cool until thermal equilibrium is achieved. Alternatively, one could start with a thermal hydrostatic equilibrium that is computed using equations (18)–(20), except that now  $F_{\text{rad}} \neq \text{const}$ . Hence, this has to be obtained by integrating  $dF_{\text{rad}}/dz = \mathcal{H}(z)$  with  $F_{\text{rad}}(z = 0) = 0$  as a boundary condition at the midplane.

For the purpose of understanding the radiative time step constraint, we will not be concerned with convection in these simulations with the PENCIL CODE. Instead, we use a one-dimensional model in which the flow is either up or down, but not both, so no return flow and no convection are possible. Convection will, however, be discussed briefly in section 4.4, where we illuminate in more detail the properties of discs around white dwarfs. In such discs, the total flux is given by  $F_{\text{tot}} = F_{\text{rad}} + F_{\text{conv}}$ , and it is found that a significant fraction of the convective flux  $F_{\text{conv}}$  is independent of the superadiabatic gradient, as is normally assumed in standard mixing length theory. This is particularly interesting in view of recent suggestions (Brandenburg 2016) that even in solar and stellar convection, the convective flux may have a significant contribution from what is known as the Deardorff (1966, 1972) term. Numerical evidence for this flux was found in simulations of stellar convection (Käpylä et al. 2017, 2018), and the convective simulations of accretion discs in this work will provide further evidence for this.

Note that we have not made any attempt to smoothen the abrupt change in the heating function of equation (25) and have rather regarded this feature as an advantage. This is because it allows us to see whether this profile results in a similarly abrupt transition in

the resulting vertical profiles of temperature or radiative flux. As will be demonstrated in section 4.3, the temperature profile turns out to be smooth, suggesting that no artifacts of the heating profile are introduced into the model. The total flux  $F_{\text{tot}}$ , on the other hand, shows a sharp first derivative in the steady state. Again, this is not a problem, since it serves as a convenient “marker” of where the heating stops in the vertical profiles of various fluxes. We will return to this in section 4.4.

Both in the stellar and in the accretion disc models, we determine the location of the photosphere as the point where the optical depth,

$$\tau(z) = \int_z^\infty \kappa(z')\rho(z') dz', \quad (26)$$

is unity. Here,  $z \rightarrow \infty$  corresponds to a location far away from the disc or the star, but for the lower disc plane, the integral would need to go from  $-\infty$  to  $z$  instead.

### 3.4. Radiation transport using long characteristics

We use here the radiation module of the PENCIL CODE as implemented by Heinemann et al. (2006). For a brief description of the most important numerical aspects, we refer the reader to section 2.4 of Barekat & Brandenburg (2014). Instead of integrating along a geometric line segment  $dl$ , we integrate equation (1) over optical depth  $d\tau = -\kappa\rho dl$  along a number of rays with direction  $\hat{n}$ , such that  $dI/d\tau = I - S$ . In formulating the boundary conditions, we distinguish between two types of rays. For rays that are perfectly horizontal, we assume periodicity. For all other rays, we normally assume that no radiation enters at the outer boundary of the domain (Mihalas 1978). However, to reproduce the analytic solution for an infinitely extended domain, we can take the layers beyond the computational domain into account if the flux is assumed to be known and the solution is in radiative equilibrium. This is explained in appendix A.

The code is parallelised by splitting the problem into two local ones and a nonlocal one in between that requires interprocessor communication. The local problems are computationally intensive, while the nonlocal problem does not involve any computations and is therefore quite fast. On each processor, one first solves equation (1) along each ray to compute the intrinsic intensity increment within each processor as a function of optical depth. In the second step, the increments of intrinsic intensity and optical depth are communicated to the neighbouring processors. In the third and final step, these increments are used to construct the total intensity within each processor. For most of the calculations presented here, we use just the vertical or  $z$  direction, which corresponds to two ray directions, namely for upward and downward propagating radiation.

## 4. Results

### 4.1. A hot stellar surface layer

We adopt here one of the stellar surface layer models of Brandenburg & Spiegel (2006, unpublished), who considered a star of solar mass  $M = M_\odot = 2 \times 10^{33}$  g and solar radius  $R = R_\odot = 7 \times 10^{10}$  cm, but with a luminosity  $L$  that is  $2 \times 10^4$  times the solar value  $L_\odot = 4 \times 10^{33}$  erg s $^{-1}$ . The radiative flux is then  $F_{\text{rad}} = L/(4\pi R^2) = 1.3 \times 10^{15}$  erg cm $^{-2}$  s $^{-1}$  and the effective temperature  $T_{\text{eff}} = 69,000$  K. Our model has a depth of 60 Mm and uses 256 uniformly spaced mesh points. The  $\tau = 1$  surface is roughly in the middle of the domain, which we define to be at  $z = 0$ . The temperature then varies between 110,000 K at  $z = -30$  Mm and 58,000 K at  $z = 30$  Mm. The sound speed varies between  $c_s = 55$  km s $^{-1}$  at the bottom and  $c_s = 42$  km s $^{-1}$  at the top, while  $c_\gamma = 55$  km s $^{-1}$  at the bottom and about  $10^8$  km s $^{-1}$  at the

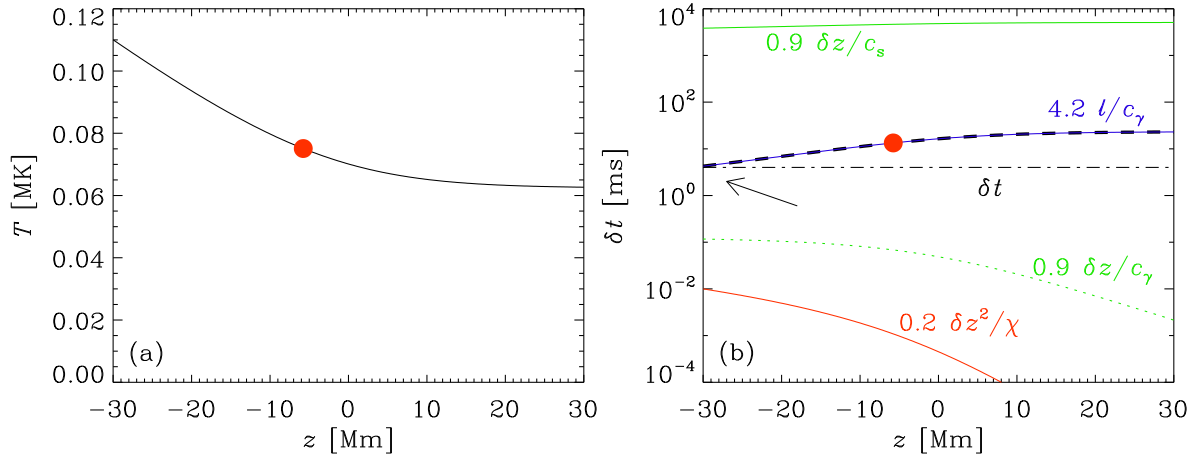


Figure 1. (a) Temperature stratification from the PENCIL CODE simulation of a hot star with  $T_{\text{eff}} = 69000\text{K}$  (see section 4.1). (b)  $z$  dependence of various time step constraints:  $\delta t_{\text{rad}}^{\text{thick}}$  (red solid line),  $\delta t_{\text{rad}}^{\text{thin}}$  (blue solid line),  $\delta t_{\text{rad}}$  (black dashed line),  $\delta t_s$  (green solid line),  $\delta t_\gamma$  (green dotted line) and the empirically determined maximum permissible time step  $\delta t$  (black dot-dashed line). The red dot denotes the photosphere. The arrow points to the location where the minimum of  $4.2\ell/c_\gamma$  coincides with  $\delta t$  and is therefore constraining the time step. All time steps are in milliseconds.

top. The domain has a density contrast of  $\rho_{\text{max}}/\rho_{\text{min}} \approx 300$ , so the number of density scale heights is  $\Delta \ln \rho = \ln 300 \approx 6$ . For the opacity we have used  $\kappa = \kappa_{\text{es}} = \text{const}$  instead of the expression given by equation (23), but the difference would be minor.

In figure 1, we show the temperature stratification for the above star, and the various candidates that could play a role in constraining the time step. We also compare with the empirically determined maximum permissible time step  $\delta t$  obtained in the PENCIL CODE simulations, which is determined as follows. Every simulation is run with a constant, pre-assigned time step. However, this simulation may become numerically unstable before a steady state solution is reached if the supplied time step is too long. One can then keep decreasing the supplied time step (to the desired accuracy) in order to determine the limiting time step for that particular problem, namely  $\delta t$  in our notation.

Interestingly, we find in figure 1 that  $\delta t$  is very close to the line for  $\delta t_{\text{rad}}^{\text{thin}} = 4.2\ell/c_\gamma$ . The line for  $\delta t_{\text{rad}}^{\text{thick}} = 0.2\delta z^2/\chi$  is well below the actual  $\delta t$ , which is consistent with equation (8) in that a term proportional to  $\delta t_{\text{rad}}^{\text{thick}}$  does not constrain  $\delta t$  in isolation. Similarly,  $\delta t_\gamma = 0.9\delta z/c_\gamma$  is not motivated to be a possible candidate for constraining the time step in this case. The acoustic time step  $\delta t_s = 0.9\delta z/c_s$  is much larger than the radiative one and therefore unimportant in this case. It is important to note here that the right-hand side of equation (9) would have predicted  $\delta t_{\text{rad}}^{\text{thick}}$  to be the relevant time step in the problem. However, in reality it turns out to be  $\delta t_{\text{rad}}^{\text{thin}}$ , as also supported by our numerical simulations.

Spiegel & Tao (1999) motivated the interest in studying the hydrodynamics of hot stars by referring to O. Struve for having discovered large line widths, which in turn could hint at the existence of turbulence in the atmospheres of those stars. They associated this line broadening with photofluid instabilities, which are possible even when the radiative acceleration is still below the gravitational one. In the present case, the radiative acceleration is 0.53 times the gravitational one, and may even exceed it at higher temperatures. This could lead to photoconvection (Prendergast & Spiegel 1973, Spiegel 1977, Spiegel & Tao 1999), which Brandenburg & Spiegel (2006, unpublished) attempted to study with the PENCIL CODE, but suspended this project because of prohibitively short time steps. In recent years, similar studies have been performed in the context of radiation-driven stellar winds (Owocki & Sundqvist 2018, Sundqvist et al. 2018). No time step problems, however, have been reported in those studies.

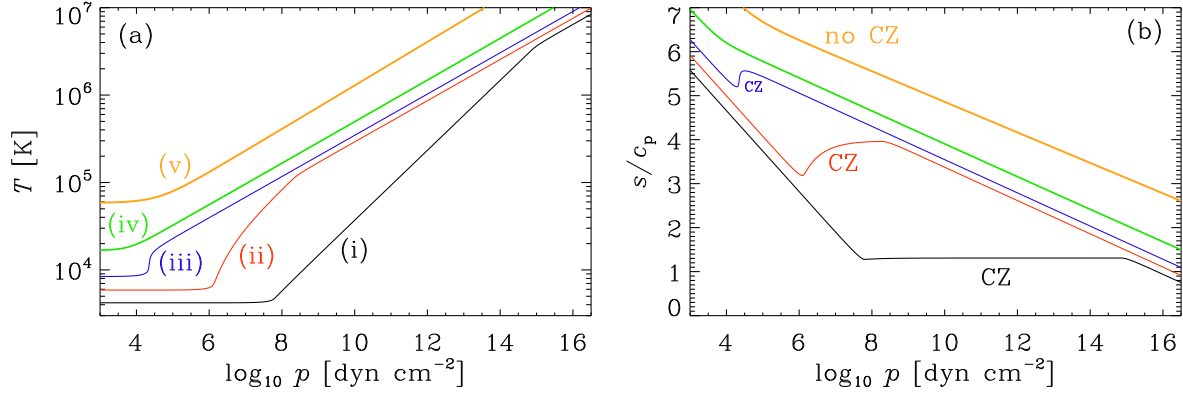


Figure 2. Temperature (a) and specific entropy (b) stratification from the mixing length model discussed in section 3.2 for  $T_{\text{eff}} = 5000$  K (i), 7000 K (ii), 10,000 K (iii), 20,000 K (iv) and  $T_{\text{eff}} = 70000$  K (v), using  $g = 2.7 \times 10^4 \text{ cm s}^{-1}$ . The locations of the convection zones are marked by CZ in three of the five curves where  $ds/d \ln p > 0$ , corresponding to a positive superadiabatic gradient.

#### 4.2. Expected time step constraints for stellar surface layers

We now consider solutions of equations (16)–(23) for stellar surface layers. In figure 2, we plot  $T(\ln p)$  and  $s(\ln p)$  for four values of  $T_{\text{eff}}$ . We use  $g = g_{\odot} = GM_{\odot}/R_{\odot}^2 = 2.7 \times 10^4 \text{ cm s}^{-1}$  (the solar value) for the following plots. In figure 3, we plot the two contributions to the radiative time step, as well as the acoustic one,

$$\delta t_{\text{rad}}^{\text{thick}} = C_{\text{rad}}^{\text{thick}} \frac{\delta z^2}{\chi}, \quad \delta t_{\text{rad}}^{\text{thin}} = C_{\text{rad}}^{\text{thin}} \frac{\ell}{c_{\gamma}}, \quad \delta t_s = C_{\text{CFL}} \frac{\delta z}{c_s}, \quad (27)$$

together with the total radiative one  $\delta t_{\text{rad}} = \delta t_{\text{rad}}^{\text{thick}} + \delta t_{\text{rad}}^{\text{thin}}$  for  $\delta z = 0.05 H_p$ , where  $H_p = (c_p - c_v)T/g$  is the local pressure scale-height in the star. In all of our models, the temperature above the photosphere reaches a constant; see figure 2(a). This is because the physics of realistic coronal heating and cooling is not included in our simple model; see the papers by Bingert & Peter (2011) and Bourdin et al. (2013) for realistic coronal modelling with the PENCIL CODE, using a setup originally developed by Gudiksen & Nordlund (2002, 2005a,b).

Next, we discuss the constraints on the resulting time step. In figure 3, at small values of  $\ln p$ , corresponding to locations above the photosphere, we have  $\delta t_{\text{rad}}^{\text{thin}} \gg \delta t_{\text{rad}}^{\text{thick}}$ , so their sum is determined by  $\delta t_{\text{rad}}^{\text{thin}}$ , as expected; see figure 3 for small values of  $\ln p$ , where the blue line for  $\delta t_{\text{rad}}^{\text{thin}}$  is the highest. In the deeper layers below the photosphere, the situation is the other way around and the time step is expected to be governed by  $\delta t_{\text{rad}}^{\text{thick}}$ , again as expected; see figure 3 for large values of  $\ln p$  (i.e., above the photosphere), where the red line for  $\delta t_{\text{rad}}^{\text{thick}}$  is the highest. The radiative time step is thus determined by the minimum of  $\delta t_{\text{rad}}$ , corresponding to the black dashed line in figure 3. We find that  $\delta t_{\text{rad}}$  is the shortest either in the photosphere [panels (a) and (b) of figure 3], indicated by a red dot where  $\tau = 1$ , or just below it [see panels (c) and (d) of figure 3, i.e., for models with shallow or no outer convection zone].

The maximum permissible time step  $\delta t$  for this problem is then given by the minimum of  $\delta t_{\text{rad}}$  and the acoustic time step  $\delta t_s$  (the green solid line). As can be seen from figure 3, for  $T_{\text{eff}} = 5000$  K, it is always  $\delta t_s$  that constrains the actual time step. Although for  $T_{\text{eff}} = 7000$  K the minimum of  $\delta t_{\text{rad}}$  occurs below the photosphere, at that location  $\delta t_s$  is still the shorter time step. However, for  $T_{\text{eff}} = 10,000$  K and higher,  $\delta t_s$  is no longer the constraining time step, instead it is  $\min(\delta t_{\text{rad}})$ . To better understand the dependence of various time steps on  $T_{\text{eff}}$  and  $g$ , we turn to table 1 and figure 4. In table 1, we give the radiative and acoustic time steps in the photosphere,  $\delta t_{\text{rad}}^{\text{phot}}$  and  $\delta t_s^{\text{phot}}$ , respectively, and the radiative and acoustic time steps at the position where the radiative time step has a minimum,  $\delta t_{\text{rad}}^{\text{deep}}$  and  $\delta t_s^{\text{deep}}$ , respectively; for the five models (i)–(v) discussed above in figures 2 and 3, and for a few other ones. In

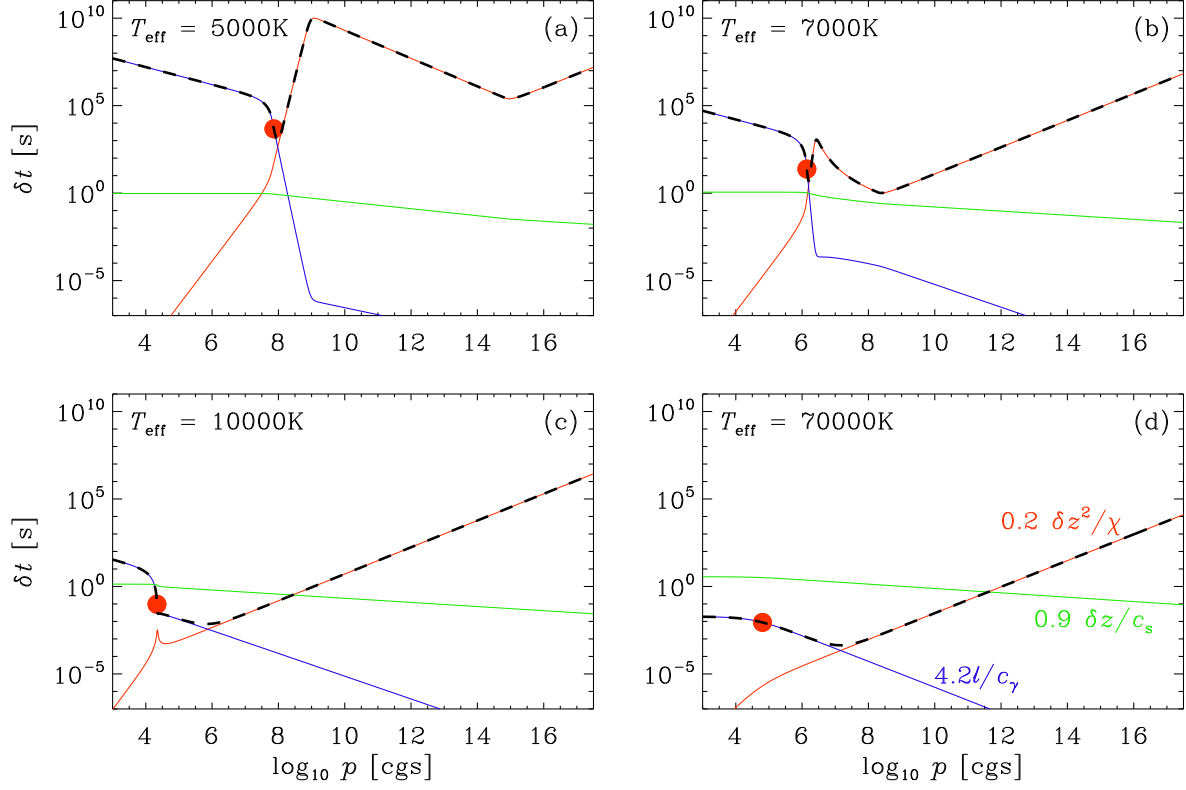


Figure 3. Time step constraint for the mixing length models (i) in panel (a), (ii) in panel (b), (iii) in panel (c) and (v) in panel (d):  $\delta t_{\text{rad}}$  (black dashed lines),  $\delta t_{\text{rad}}^{\text{thin}}$  (blue solid lines),  $\delta t_{\text{rad}}^{\text{thick}}$  (red solid lines), and  $\delta t_s$  (green solid lines). All time steps are in seconds.

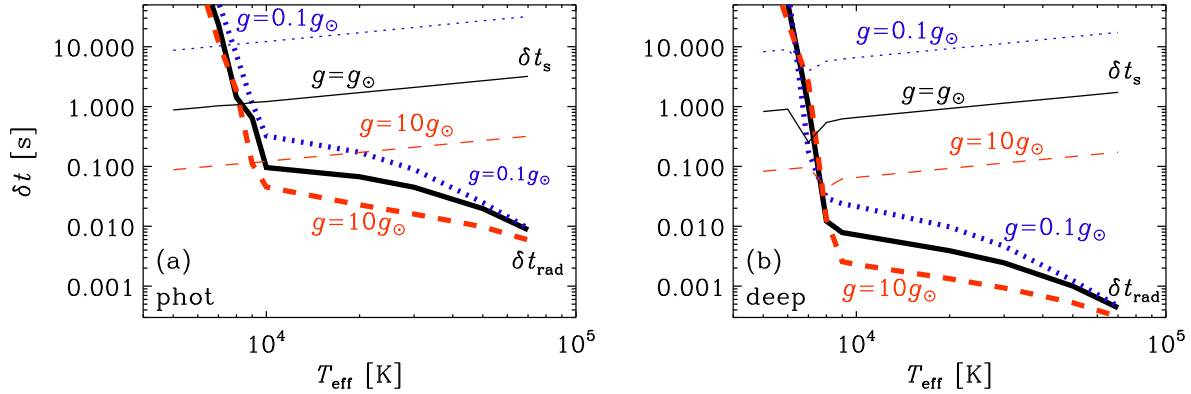


Figure 4.  $\delta t_{\text{rad}}$  and  $\delta t_s$  at the photosphere (a) and at the location where  $\delta t_{\text{rad}}$  is minimum (b) for  $g = g_{\odot} = 2.7 \times 10^4 \text{ cm s}^{-2}$  (black solid lines),  $g = 0.1 g_{\odot}$  (blue dotted lines), and  $g = 10 g_{\odot}$  (red dashed lines). The thick and thin lines correspond to  $\delta t_{\text{rad}}$  and  $\delta t_s$  respectively. All time steps are in seconds.

figure 4, we plot these newly defined time steps as a function of  $T_{\text{eff}}$  for different values of  $g$ .

We see from table 1 and figure 4 clearly that as  $T_{\text{eff}}$  increases for a given  $g$ , the radiative time steps (thick lines) decrease whereas the acoustic time steps (thin lines) increase (both in the photosphere and deeper layers). We find that for stars with  $T_{\text{eff}} < 10,000 \text{ K}$ ,  $\delta t_s$  gives the time step constraint, whereas for stars with  $T_{\text{eff}} \gtrsim 10,000 \text{ K}$ ,  $\delta t_{\text{rad}}$  is the more constraining one. Note that this segregation of the cold and hot stellar branches at  $T_{\text{eff}} \approx 10,000 \text{ K}$  seen in the  $\delta t_{\text{rad}}$  curves of figure 4 is a consequence of our opacity prescription given by equation (24). In equation (24), we use  $T_0 = 13,000 \text{ K}$ , such that the stars hotter than this are described

predominantly by Kramers opacity and stars cooler than this by  $\text{H}^-$  opacity. We see from figure 4 that for a given  $g$ , the  $\delta t_s$  and  $\delta t_{\text{rad}}$  curves intersect at a particular  $T_{\text{eff}}$ , which is typically  $< 10,000$  K; for e.g. the thin and thick red dashed lines in panel (a) intersect at  $\sim 9000$  K. These stars are in fact the most economical to simulate numerically, as  $\delta t_s \approx \delta t_{\text{rad}}$  and one does not need to worry about conflicting time steps in the problem. For hotter stars, however, we see that the  $\delta t_s$  and  $\delta t_{\text{rad}}$  diverge more and more away from each other, thus leading to a problem. For a given  $T_{\text{eff}}$ , we see that  $\delta t_s$  always decreases with increasing  $g$ . The  $\delta t_{\text{rad}}$  curves for a given  $T_{\text{eff}} < 10,000$  K, on the other hand, seem to be nearly independent of  $g$ . However, as  $T_{\text{eff}}$  increases beyond  $10,000$  K, we find that the more massive stars have a shorter radiative time step. Interestingly, as  $T_{\text{eff}} \rightarrow 10^5$  K,  $\delta t_{\text{rad}}$  again starts to become independent of  $g$ . Note that the time steps in the deeper layers of the star, as shown in figure 4(b) are much shorter than their photospheric counterparts, especially for hot massive stars. This also poses a numerical challenge if one wishes to simulate such a star all the way from the deeper layers up to the photosphere.

Finally, we confirm that the stratification in the present hydrostatic models agrees with that obtained in section 4.1 using the PENCIL CODE. We do so by comparing the locations of the photosphere in figures 1 and 3(d), both of which correspond to the model having  $T_{\text{eff}} \sim 70,000$  K. We note from figure 1 that the computational domain ranges from  $z = -30$  Mm to  $+30$  Mm, with the negative values representing the deeper layers of the star. The corresponding  $\log_{10} p$  varies from 2.75 to 5.47 across the domain, where  $p$  is in cgs units. In figure 1, the photosphere ( $\tau = 1$ ) is at  $z = -5.8$  Mm or  $\log_{10} p = 4.6$ , which indeed is in excellent agreement with the location of the photosphere in figure 3(d). Also, the value of  $\delta t_{\text{rad}}$  at the photosphere agrees between figures 1 and 3(d), being  $\approx 10^{-2}$  s in both (keeping in mind that the time step in figure 1 is given in milliseconds). We make a note here regarding the location of the minimum of the radiative time step in theoretical models versus numerical computation. We see from figure 3(d) that  $\min(\delta t_{\text{rad}})$  occurs in the deeper layers at  $\log_{10} p \approx 7.2$ , which is in fact outside the computational domain of interest in figure 1. It is only for the cool stars, that the photosphere coincides with the location of  $\min(\delta t_{\text{rad}})$ ; see e.g. figure 3(a).

Table 1.  $\delta t_{\text{rad}}$  and  $\delta t_s$  at the photosphere (superscript ‘phot’) and at the location where  $\delta t_{\text{rad}}$  is minimum (superscript ‘deep’) for some values of  $T_{\text{eff}}$  and  $g$ . All time steps are given in seconds.

Model	$T_{\text{eff}}$	$g/g_{\odot}$	$\delta t_{\text{rad}}^{\text{phot}}$	$\delta t_s^{\text{phot}}$	$\delta t_{\text{rad}}^{\text{deep}}$	$\delta t_s^{\text{deep}}$
(i)	5,000	1	$4.7 \times 10^{+3}$	0.88	$8.5 \times 10^{+2}$	0.83
	6,000	1	$2.5 \times 10^{+2}$	0.95	$5.4 \times 10^{+1}$	0.90
	7,000	1	$2.4 \times 10^{+1}$	1.03	$1.0 \times 10^{+0}$	0.25
(ii)	8,000	1	$1.4 \times 10^{+0}$	1.07	$1.2 \times 10^{-2}$	0.54
	9,000	1	$6.4 \times 10^{-1}$	1.17	$7.9 \times 10^{-3}$	0.62
(iii)	10,000	1	$9.6 \times 10^{-2}$	1.21	$7.2 \times 10^{-3}$	0.66
(iv)	20,000	1	$6.7 \times 10^{-2}$	1.71	$3.9 \times 10^{-3}$	0.93
	30,000	1	$4.5 \times 10^{-2}$	2.09	$2.5 \times 10^{-3}$	1.14
	50,000	1	$2.0 \times 10^{-2}$	2.70	$1.0 \times 10^{-3}$	1.46
(v)	70,000	1	$8.8 \times 10^{-3}$	3.20	$4.4 \times 10^{-4}$	1.73
(iii)	10,000	0.1	$3.2 \times 10^{-1}$	12.2	$2.2 \times 10^{-2}$	6.57
	10,000	1	$9.6 \times 10^{-2}$	1.21	$7.2 \times 10^{-3}$	0.66
	10,000	10	$4.5 \times 10^{-2}$	0.12	$2.3 \times 10^{-3}$	0.07

### 4.3. DNS results for disc models

In our earlier exploratory models (Brandenburg & Das, unpublished), we solved the disc models for both the upper and lower disc plane, but in the subsequent models presented below, we have restricted ourselves to solving the equations in just the upper disc plane by assuming a symmetry condition at  $z = 0$ . These solutions are identical to our earlier ones and computationally more economic. For the initial isothermal stratification used here (as discussed in section 3.3), the pressure and density scale heights are identical, so  $H_p = H_\rho$ , but in general they are somewhat different from each other; see appendix B.

We consider one-dimensional solutions of equations (10)–(13) for a fixed value of the vertically integrated (surface) density  $\Sigma = \int_{-\infty}^{\infty} \rho dz$ . In our horizontally periodic domains with horizontal extent  $L_x \times L_y$ , the total mass is  $\Sigma L_x L_y$ , which is conserved and therefore given by the initial conditions. We use  $\Sigma = 7 \times 10^{-6} \text{ g cm}^{-3} \text{ Mm}$ , and two values for  $\mathcal{H}_0 = \mathcal{H}(z = 0)$ , namely,  $\mathcal{H}_0 = 2 \times 10^{-6} \text{ g cm}^{-3} \text{ km}^3 \text{ s}^{-3} \text{ Mm}^{-1}$  (cold disk) and  $\mathcal{H}_0 = 5 \times 10^{-5} \text{ g cm}^{-3} \text{ km}^3 \text{ s}^{-3} \text{ Mm}^{-1}$  (hot disk). In cgs units, our values correspond to  $\Sigma = 7 \times 10^2 \text{ g cm}^{-2}$ ,  $\mathcal{H}_0 = 20 \text{ g cm}^{-1} \text{ s}^{-3}$ , and  $\mathcal{H}_0 = 500 \text{ g cm}^{-1} \text{ s}^{-3}$ , which are appropriate values for discs in cataclysmic variables. These were chosen based on preliminary calculations of semi-analytically constructed models relevant to the regime where multi-valued solutions of  $\dot{M}$  (or equivalently  $\mathcal{H}_0$  in our formalism) are possible for a given  $\Sigma$ . These solutions are governed by the hydrogen ionisation instability that lead to the so called disc instability model of cataclysmic variables; see Lasota (2001) for a review. Note that for PENCIL CODE simulations, it is convenient to measure lengths in units of Mm, speed in  $\text{km s}^{-1}$ , and density in  $\text{g cm}^{-3}$ , which explains our choice of units adopted in the results presented here.

We first discuss figure 5, where we present the solutions for a cold accretion disk. In this case,  $T$  varies from a photospheric value of about 2600 K to about 3700 K in the midplane; see panel (a). Here we choose a vertical domain size of  $L_z = 1 \text{ Mm}$ . In panels (c) and (d), we plot the various time steps for two vertical grid resolutions  $N_z = 144$  and 576. According to our reasoning in section 2, the radiative time step should be limited by the sum of  $\delta t_{\text{rad}}^{\text{thin}}$  and  $\delta t_{\text{rad}}^{\text{thick}}$ . However, for the cold disc solution, the former is much larger.  $\delta t_{\text{rad}}^{\text{thin}}$  reaches values of between  $10^{-2}$  ks in the midplane and increases to  $10^{-1}$  ks in the outer layers (for both  $N_z = 144$  and 576 as it is independent of  $\delta z$ ), and, hence it determines the radiative time step  $\delta t_{\text{rad}}$ . The maximum permissible empirically determined time step  $\delta t$ , on the other hand, is only around  $10^{-3}$  ks for  $N_z = 144$ , and  $1.8 \times 10^{-4}$  ks for  $N_z = 576$ . It turns out that this value is entirely explained by the standard CFL condition, where the time step is limited by the acoustic time step  $\delta t_s$ ; compare black dot-dashed and green solid lines in figures 5(c) and (d). From panel (b) we see that  $c_\gamma$  is well below  $c_s$  throughout the computational domain. It varies only between  $1.6 \text{ km s}^{-1}$  in the photosphere to about  $2.6 \text{ km s}^{-1}$  in the midplane, and reaches  $6 \text{ km s}^{-1}$  in the outermost parts well above the photosphere. The relevance of the ratio  $c_s/c_\gamma$  will become more clear in section 5.

In figure 6, we present the hot disk solutions for  $N_z = 144$  and 576, where  $T$  varies from a photospheric value of 5000 K to about 32,000 K in the midplane. We choose  $L_z = 4 \text{ Mm}$  for this case, which extends from the midplane to a point somewhat above the photosphere. We find from panels (c) and (d) that the hot disc behaves somewhat similarly to the stellar surface layers discussed in section 4.2, where  $\delta t_{\text{rad}}$  in the layers at some depth beneath the photosphere is governed by  $\delta t_{\text{rad}}^{\text{thick}}$  (solid red line), while in the outer layers by  $\delta t_{\text{rad}}^{\text{thin}}$  (solid blue line). The minimum of the total radiative time step, however, occurs at the midplane, such that  $\min(\delta t_{\text{rad}}) \sim 10^{-4}$  ks for  $N_z = 144$ , and  $\sim 7 \times 10^{-6}$  ks for  $N_z = 576$ . This is very much consistent with the maximum permissible empirical time step  $\delta t$ , which is  $\sim 6 \times 10^{-5}$  ks for  $N_z = 144$  and  $\sim 7 \times 10^{-6}$  ks for  $N_z = 576$ . Note that  $\delta t_{\text{rad}}^{\text{thick}}$  is much more stringent in this case and limits the time step; compare the red solid and black dot-dashed lines in figure 6(d). Also,  $\delta t_{\text{rad}}^{\text{thick}} \propto \delta z^2$ , as can be seen from panels (c) and (d) of both figures 5 and 6. The standard CFL

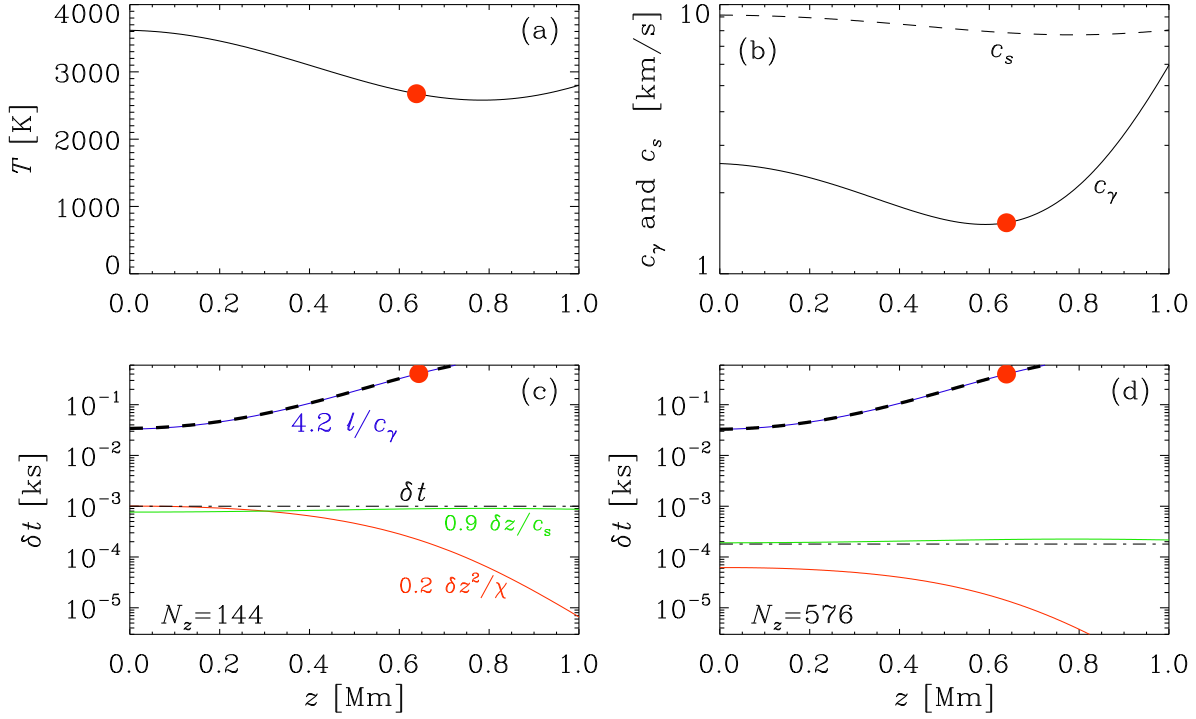


Figure 5. Vertical profiles of  $T$  (a), and  $c_\gamma$  and  $c_s$  (b).  $\delta t_{\text{rad}}^{\text{thin}}$  (blue lines),  $\delta t_{\text{rad}}^{\text{thick}}$  (red lines), their sum  $\delta t_{\text{rad}}$  (thick dashed lines),  $\delta t_s$  (green solid lines), and  $\delta t$  (black dot-dashed lines) for the cold disc model discussed in section 4.3, with  $N_z = 144$  (c) and  $N_z = 576$  (d). All time steps are in kiloseconds.

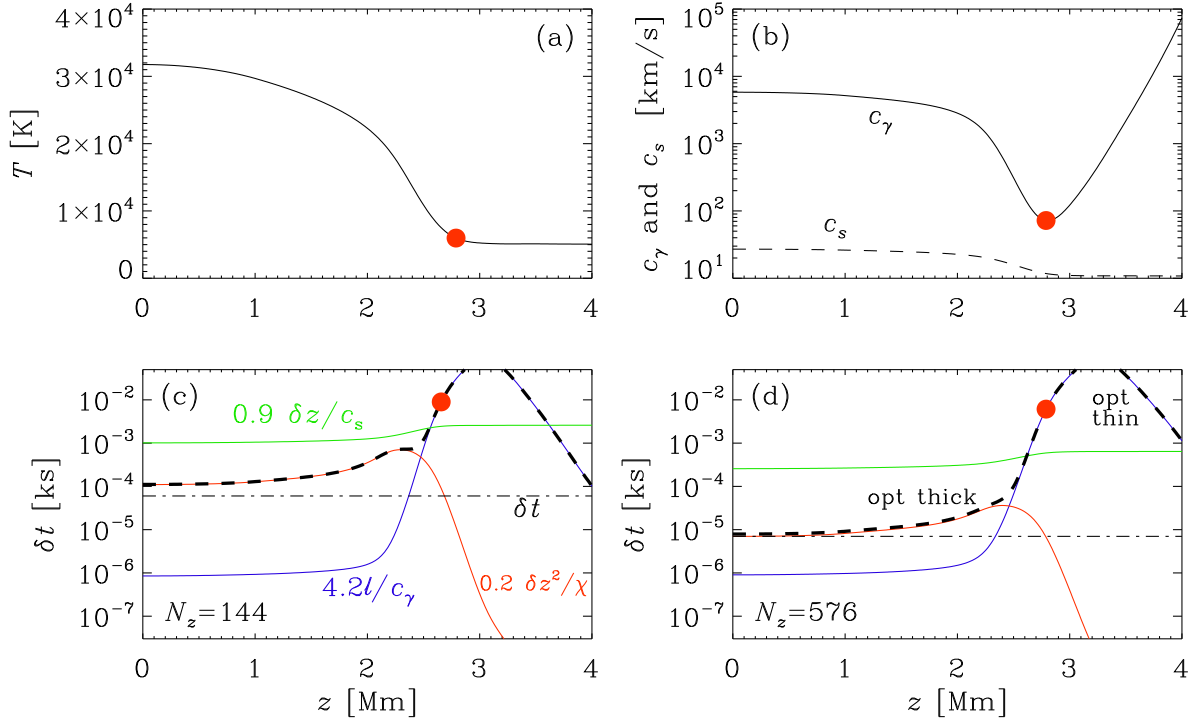


Figure 6. Same as figure 5, but for the hot disc model discussed in section 4.3. All time steps are in kiloseconds.

condition is not relevant to explain  $\delta t$  in this case as  $\delta t_s > \min(\delta t_{\text{rad}})$ . Furthermore,  $c_\gamma > c_s$  throughout the domain, reaching about  $7000 \text{ km s}^{-1}$  in the midplane and even  $10^5 \text{ km s}^{-1}$  in

the outer layers; see figure 6(b). We will return to the effect of this in section 5.

Finally, we discuss table 2, where we summarise the empirically determined maximally permissible time step  $\delta t$  for the cold and hot disk models. We also compare with the numerically determined values of  $\chi_0 \delta t / \delta z^2$  and  $c_{s0} \delta t / \delta z$ , which will help us constrain the coefficients  $C_{\text{rad}}^{\text{thick}}$  and  $C_{\text{CFL}}$ , respectively (the subscript 0 indicates the values of the respective quantities at the disc midplane). From the cold disk solutions, where the time step is constrained by  $\delta t_s$ , we find that  $c_{s0} \delta t / \delta z = 1.3$  for  $N_z = 144$ , and  $c_{s0} \delta t / \delta z = 0.95$  for  $N_z = 576$ . These values are very close to the value of the standard Courant factor used in the PENCIL CODE. Hence, we can conclude that  $C_{\text{CFL}} = 0.95$ , which is also consistent with the value of 0.9, which was adopted while plotting figure 5. Note that ideally these values should be independent of resolution, but in practice they do seem to depend on it. We hence adopt the smaller of the two values as the more restrictive constraint. From the hot disk solutions, where the time step is constrained by  $\delta t_{\text{rad}}^{\text{thick}}$ , we hope to constrain the coefficient  $C_{\text{rad}}^{\text{thick}}$ . First we find that for this case,  $c_{s0} \delta t / \delta z \ll 1$ , which is contrary to our understanding of the CFL coefficient and, hence, we discard these values. Comparing the values of  $\chi_0 \delta t / \delta z^2$ , we conclude that  $C_{\text{rad}}^{\text{thick}} = 0.19$ , since this is the smallest of the two resolutions. This value is also consistent with our choice of 0.2, which was used while plotting figure 6. Note that neither the hot disk nor the cold disk models are suitable for determining the coefficient  $C_{\text{rad}}^{\text{thin}}$ , as  $\delta t_{\text{rad}}^{\text{thin}}$  never constrains the time step in these cases. However, the value of  $C_{\text{rad}}^{\text{thin}} = 4.2$  that we obtained from our zero-dimensional experiment and used for the our plots, is indeed consistent with the simulation results reported in section 4.1; see also figure 1.

#### 4.4. Three-dimensional DNS of discs with vertical heating profile

In section 3.3, we introduced the heating profile  $\mathcal{H}(z)$  and stated that the discontinuity at  $z = \pm z_{\text{heat}}$  does not cause any artefacts, that the thermodynamic variables such as temperature and specific entropy are smooth, and that only the energy flux shows sharp corners at  $z = \pm z_{\text{heat}}$ . This is demonstrated in figure 7, where we show the results for a three-dimensional model with an intermediate heating source  $\mathcal{H}_0 = 10^{-5} \text{ g cm}^{-3} \text{ km}^3 \text{ s}^{-3} \text{ Mm}^{-1}$  in a cubic domain  $[L_x, L_y, L_z]$  of size  $(4 \text{ Mm})^3$ , covering both the lower and upper disc planes, using  $576^3$  mesh points and a coefficient for the shock viscosity of  $C_{\text{shock}} = 0.5$ .

The temperature reaches a maximum of 9000 K at  $z = 0$  and has an approximately flat profile away from the lower and upper photospheres. It turns out that the temperature profile is not perfectly flat. This can probably be ascribed to the long thermal adjustment time in this system, which we can estimate as follows. The Kelvin–Helmholtz timescale is given by  $\tau_{\text{KH}} = E_{\text{th}} / L$ , where  $E_{\text{th}} = \int \rho c_v T dV$  is the internal energy,  $L = 2F_{\infty} L_x L_y = 2\mathcal{H}V$  is the luminosity for the losses on both photospheres,  $V = L_x L_y L_z$  is the volume of the domain, and  $F_{\infty}$  is the value of the total flux in the photosphere. Using  $E_{\text{th}} = \Sigma L_x L_y \overline{c_s^2} / [\gamma(\gamma - 1)]$  with  $\overline{c_s^2} \equiv \langle \rho c_s^2 \rangle / \langle \rho \rangle \approx (13 \text{ km/s})^2$ , and  $[\gamma(\gamma - 1)]^{-1} = 0.9$  for  $\gamma = 5/3$ , we have  $\tau_{\text{KH}} = 0.45 \overline{c_s^2} \Sigma / \mathcal{H}_0 L_z = 50 \text{ ks}$ , which is about three times longer than the duration of our simulation.

The specific entropy,  $s/c_p = \ln(T/p^{\nabla_{\text{ad}}})$ , has a negative slope,  $ds/d \ln z < 0$ , corresponding to

Table 2. Empirical time step  $\delta t$  obtained from the one dimensional cold and hot disk simulations shown in figures 5 and 6;  $\chi_0$  is given in  $\text{Mm km s}^{-1}$ ,  $c_{s0}$  in  $\text{km s}^{-1}$ , and  $\delta t$  in ks, where  $\chi_0$  and  $c_{s0}$  denote values at the disc midplane. The bold face values indicate the time step constraints obtained for  $C_{\text{rad}}^{\text{thick}}$  and  $C_{\text{CFL}}$ .

			$N = 144$			$N = 576$		
	$\chi_0$	$c_{s0}$	$\delta t$	$\chi_0 \delta t / \delta z^2$	$c_{s0} \delta t / \delta z$	$\delta t$	$\chi_0 \delta t / \delta z^2$	$c_{s0} \delta t / \delta z$
Cold	0.017	9.1	$1.0 \times 10^{-3}$	0.35	1.3	$1.8 \times 10^{-4}$	1.0	<b>0.95</b>
Hot	2.5	27	$6 \times 10^{-5}$	<b>0.19</b>	0.06	$7 \times 10^{-6}$	0.35	0.03

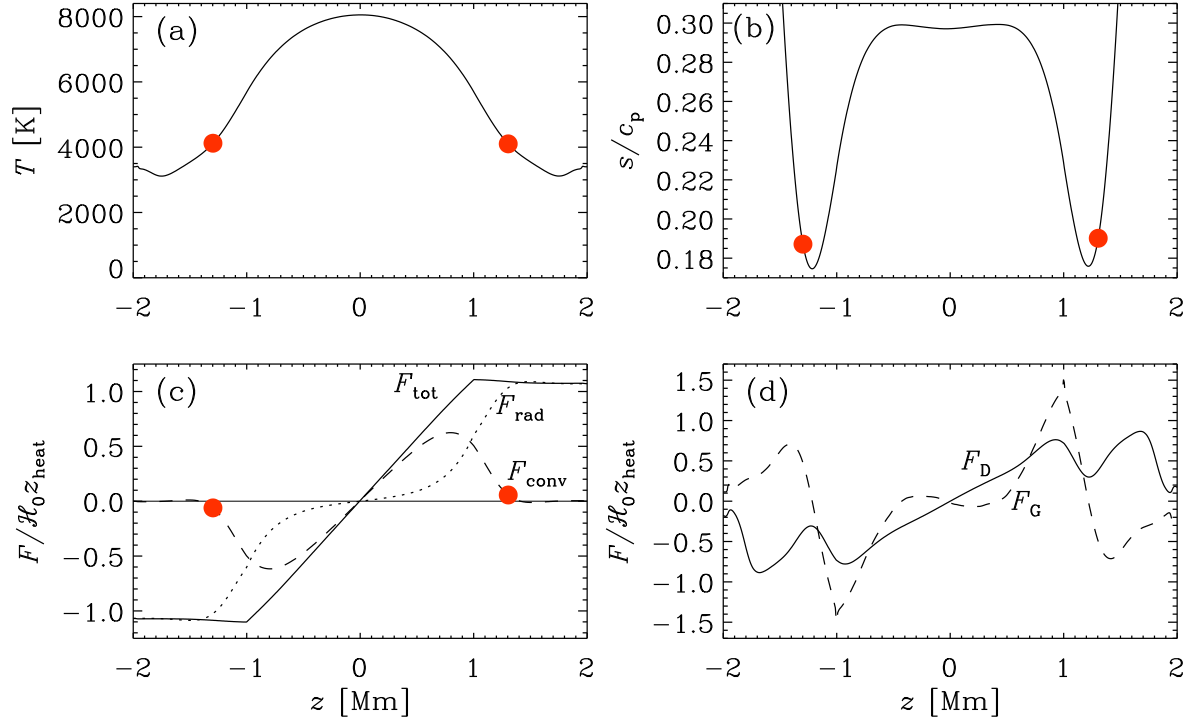


Figure 7. Temperature (a) and specific entropy (b) along with the various fluxes normalised by  $\mathcal{H}_0 z_{\text{heat}}$  (c) and (d), for a model with  $\Sigma = 7.2 \times 10^{-7} \text{ g cm}^{-3} \text{ Mm}$  and  $\mathcal{H}_0 = 10^{-5} \text{ g cm}^{-3} \text{ km}^3 \text{ s}^{-3} \text{ Mm}^{-1}$ .

a Schwarzschild-unstable stratification. This should lead to instability and hence to turbulent convection. This is indeed the case as seen in figure 7(c), where we plot the mean energy fluxes averaged over a time span when the system is in an approximately steady state between  $t = 15 \text{ ks}$  and  $20 \text{ ks}$ , which is still subject to slow thermodynamic adjustments on the longer timescale  $\tau_{\text{KH}} = 50 \text{ ks}$ . In particular, we plot  $F_{\text{rad}}$  together with  $F_{\text{conv}}$  and  $F_{\text{tot}} = F_{\text{rad}} + F_{\text{conv}}$ , where  $F_{\text{conv}} = F_{\text{enth}} + F_{\text{kin}}$ , with

$$F_{\text{enth}} = \overline{\rho u_z c_p T}, \quad F_{\text{kin}} = \overline{\rho u_z \mathbf{u}^2 / 2}, \quad (28)$$

being the enthalpy and kinetic energy fluxes, and overbars denote from now on horizontal  $xy$  averages.

Note that in figure 7,  $F_{\text{tot}}$  varies approximately linearly in  $|z| < z_{\text{heat}}$  and then reaches a plateau with  $F_{\text{tot}} = \pm F_{\text{tot}}^\infty$  on both ends. However,  $F_{\text{tot}}^\infty / \mathcal{H}_0 z_{\text{heat}} \approx 1.2$  exceeds the expected values of  $\pm 1$ , which is, again, indicative of the simulation still not being in thermal equilibrium. The radiative flux is small near the midplane and energy is mostly carried by convection. The kinetic energy is not plotted, but it is about 10% of the convective flux and directed opposite to it, i.e., inward. This is a well known consequence of the up-down asymmetry of compressible convection (Hurlburt et al. 1984).

We see that in the inner parts of the disk, i.e., for  $|z| < 0.5 \text{ Mm}$ , most of the energy is carried by convection. This is curious in view of the fact that the stratification in those parts is close to adiabatic. Therefore, the standard mixing length prescription of the convective flux being carried by a gradient term,  $F_{\text{enth}} \approx F_{\text{G}}$  with (e.g. Rüdiger 1989)

$$F_{\text{G}} = -\chi_{\text{turb}} \bar{\rho} \bar{T} \nabla \bar{s}, \quad (29)$$

where  $\chi_{\text{turb}} \approx u_{\text{rms}} H_p / 3$ , cannot hold. As argued in Brandenburg (2016), the reason for this is that there is another important term, the Deardorff term, resulting from entropy fluctuations

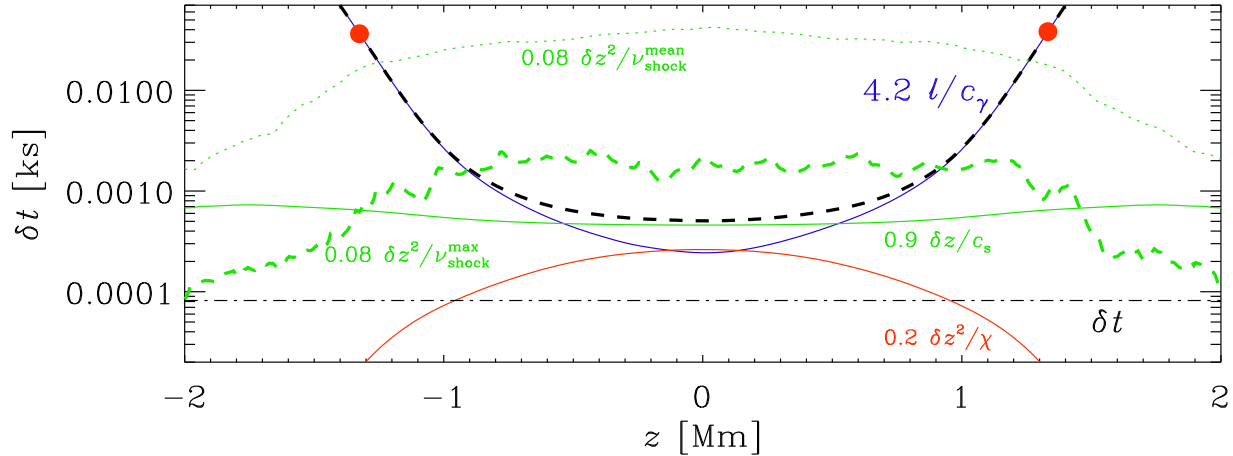


Figure 8.  $z$  dependence of the various time steps for the three-dimensional convective accretion disc simulation with  $\Sigma = 7 \times 10^{-6} \text{ g cm}^{-3} \text{ Mm}$  and  $\mathcal{H}_0 = 10^{-5} \text{ g cm}^{-3} \text{ km}^3 \text{ s}^{-3} \text{ Mm}^{-1}$ .  $\delta t_{\text{rad}}^{\text{thin}}$  (blue solid line),  $\delta t_{\text{rad}}^{\text{thick}}$  (red solid line), their sum  $\delta t_{\text{rad}}$  (black dashed line),  $\delta t_s$  (green solid line), the time step due to the maximum shock viscosity ( $0.08 \delta z^2 / \nu_{\text{shock}}^{\text{max}}$ ; green dashed line), the time step due to mean shock viscosity ( $0.08 \delta z^2 / \nu_{\text{shock}}^{\text{mean}}$ ; green dotted line), and the empirical time step  $\delta t$  (black dot-dashed line). All time steps are in kiloseconds.

(Deardorff 1966, 1972),

$$F_{\text{D}} = -\overline{\tau s'^2} \mathbf{g} / c_p, \quad (30)$$

where we have ignored the possibility of factors of the order of unity. Likewise, in equation (29), there could also be such factors, so we cannot expect perfect agreement between  $F_{\text{conv}}$  and the contributions  $F_{\text{G}}$  and  $F_{\text{D}}$  shown in figure 7(c). We do see, however, that  $F_{\text{D}}$  increases approximately linearly in the bulk of the disc ( $|z| < 0.5 \text{ Mm}$ ), while  $F_{\text{G}}$  does not even have the correct sign in order to explain  $F_{\text{conv}}$ . This is strong evidence that convection in such discs must be described by the Deardorff term. Similar results have previously only been found from stellar convection simulations (Käpylä et al. 2017, 2018).

Returning to the topic of this paper, we now investigate the various times step constraints for this model. In figure 8, similar to our earlier plots, we show the various times steps, but now we also plot the time step constraint from viscosity, particularly the one from shock viscosity. It turns out that the minimum of radiative and acoustic time steps are approximately equal ( $\approx 5 \times 10^{-4} \text{ ks}$ ) and occur in the disk midplane ( $z = 0$ ). However, the most severe time step constraint comes, in this case, from the outer layers above the photosphere, where the shock viscosity is large.

To appreciate the reason for such shocks to occur, we now look at the  $xz$  cross sections of  $u_x$ ,  $u_y$ , and  $u_z$  shown in figure 9. We see that the flow possesses two major pairs of up- and down-draughts. These cross sections were taken at  $y = 0$ , but different cross sections for different values of  $y$  look qualitatively similar, indicating that the large-scale structure is independent of  $y$ . Away from the both photospheres, however, significant velocities are still possible, which can lead to the formation of shocks in those parts. These are best seen in the image of  $u_x$ ; see first panel of figure 9. The arrow points to the strongest shock near  $z = -2 \text{ Mm}$ , where the local Mach number, i.e., the ratio of velocity to sound speed, reaches values of around 1.3.

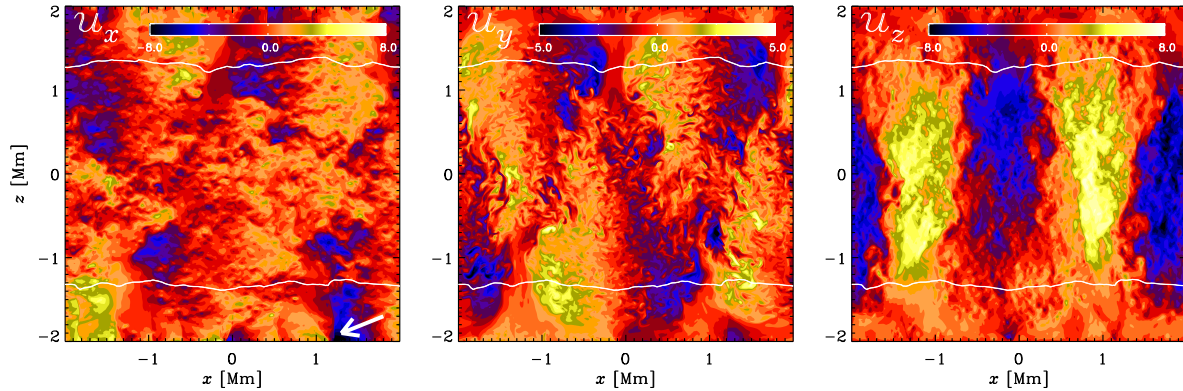


Figure 9.  $xz$  cross sections of  $u_x$ ,  $u_y$ , and  $u_z$  for the three-dimensional convective accretion disc simulation with  $\Sigma = 7 \times 10^{-6} \text{ g cm}^{-3} \text{ Mm}$  and  $\mathcal{H}_0 = 10^{-5} \text{ g cm}^{-3} \text{ km}^3 \text{ s}^{-3} \text{ Mm}^{-1}$ . The white lines show the  $\tau = 1$  surfaces and the arrow points to the strongest shock near  $z = -2 \text{ Mm}$ .

## 5. Approaches to mitigating the radiative time step problem

There appears to be a general problem with hot stars and accretion discs where the radiative time step is much shorter than the acoustic one. This is either because

$$4.2 \ell / c_\gamma \ll 0.9 \delta z / c_s \quad (\text{problem A}), \quad (31)$$

as in section 4.1, or because

$$0.2 \delta z^2 / \chi \equiv 0.6 \delta z^2 / c_\gamma \ell \ll 0.9 \delta z / c_s \quad (\text{problem B}), \quad (32)$$

as in section 4.3. In both cases, the problem is caused by the smallness of  $c_s/c_\gamma$  compared with the value of  $\delta z/4.2\ell$  in problem A or the value of  $\ell/0.6\delta z$  in problem B. In problem A,  $c_s/c_\gamma$  becomes as small as  $10^{-6}$ , as seen by comparing the green solid and dotted lines at the outer edge of the computational domain in figure 1(b). While in problem B,  $c_s/c_\gamma$  drops to  $10^{-4}$  at the outer edge of the disc, as seen in figure 6(b). For problem A, the photospheric value of  $\delta z/4.2\ell$  is about 0.006, as calculated from the model discussed in figure 1. While for problem B, the photospheric value of  $\ell/0.6\delta z$  is about 16, as calculated from the model discussed in figure 6(d). Note that these are both quite large compared to the respective  $c_s/c_\gamma$  values.

To discuss ways of mitigating the time step problem, we must distinguish the two cases A and B. For problem B, the difficulty appears through the optically thick constraint in the part where convection would develop in the three-dimensional simulations, as discussed in section 4.4; see also figure 9. Thus, radiation should not be physically important and it would be unreasonable to spend much computational resources on this. One may therefore adopt the approach of artificially increasing the opacity in that part, so that  $\chi = c_s \ell / 3 = c_s / 3 \kappa \rho$  becomes smaller and, as a consequence, the optically thick time step becomes longer. This would increase the fractional convective flux, but not the total flux.

For problem A, on the other hand, it is important to maintain a large radiation pressure in order to study photoconvection and, hence,  $\kappa F_{\text{rad}}/cg$  should be close to unity. Here, however, increasing  $\kappa$  would be counterproductive, because the relevant time step is  $4.2 \ell / c_\gamma$ , which would become even smaller as  $\ell \propto 1/\kappa$ . Thus, we have the problem that, on the one hand,  $\kappa F_{\text{rad}}/cg$  should be close to unity and certainly not be too small, and on the other hand,  $4.2 \ell c_s / (0.9 \delta z c_\gamma)$  should also be close to unity so that the acoustic and optically thin radiative time steps are close together; see equation (31). Combining these two constraints, we want to

ensure that the

$$\text{product of two constraints} = \underbrace{\frac{4.2 \ell}{0.9 \delta z} \frac{c_s}{c_\gamma}}_{\text{time step}} \underbrace{\frac{\kappa F_{\text{rad}}}{cg}}_{\text{photoconv}} \quad (33)$$

is as close to unity as possible because we want  $\kappa F_{\text{rad}}/cg \gg 1$ . Using  $F_{\text{rad}} \approx \sigma_{\text{SB}} T^4$ ,  $\delta z \approx 0.05 H_p$ , and  $\kappa \rho \ell = 1$ , we find that the

$$\text{product of two constraints} = \frac{4.7 c_s}{0.05 \cdot 16 \nabla_{\text{ad}} c} \approx 15 c_s/c. \quad (34)$$

Thus, it is clear that the best chance of studying photoconvection in hot massive stars is in the relativistic regime, because then the right hand side of equation (34) is close to unity. Alternatively, of course, one may just take a solar-type model, where the radiative and acoustic time steps are already close together, but then decrease  $c$  artificially, in order to boost the radiative pressure. Such models have, to the best of our knowledge, not yet been studied.

## 6. Conclusions

Our work has demonstrated quantitatively how the maximally permissible time step varies with  $\delta z^2/\chi$  in the optically thick regime and with  $\ell/c_\gamma$  in the optically thin one. In particular, we have shown that the radiative time step is governed by the sum of the optically thick and thin constraints, and not by the smaller of the two, as one might have naively expected by analogy with other time step constraints entering the problem.

By covering stellar surface models in the Hertzsprung–Russell (HR) diagram, we get a comprehensive understanding of which of the two constraints decide about the limiting time step. This showed that the most severe constraint on the radiative time step occurs for larger values of  $g$  and  $T_{\text{eff}}$ , which corresponds to the lower left corner of the HR diagram. In this connection, we recall that in theoretical HR diagrams, increasing luminosity is replaced by decreasing surface gravity; see, e.g., Trampedach et al. (2013). We have also seen that, for the cool stars with  $T_{\text{eff}} \lesssim 5000$  K the location of the minimum radiative time step coincides with the location of the photosphere. This is not true for hotter stars, where the minimum radiative time step occurs in the deeper layers. For accretion discs (both hot and cold), on the other hand, the shortest radiative time step tends to occur in the midplane.

The examples presented in this paper highlight some of the difficulties in dealing with global simulations by covering regimes where different time step constraints prevail. It is clear that the optimal approach would be one where different regions in space would not only have to have different spatial resolutions, but also different time steps. This would save resources that can at the same time be used to speed up the calculation in regions that require shorter time steps. A code satisfying such requirements is the DISPATCH code (Nordlund et al. 2018). Nevertheless, the time step constraints discussed in the present paper should apply to such codes just as well.

For the three dimensional accretion disk model presented here, the temperatures are moderate, and the acoustic and radiative time step constraints are about equally short. This happens in the midplane. In the outer parts, above the two photospheres, shocks become important. The time step constraint resulting from the shock viscosity is here about equally severe as the acoustic and radiative ones in the disk midplane. In such a situation, one might not gain much by using an implicit scheme, or by adopting a code that treats different regions in space with different time steps. However, it is important to monitor the various time step constraints carefully and try to stay close to physical regimes in which the different constraints are not vastly different from each other. This way the simulation can utilise existing resources in an

optimal way.

### Acknowledgements

This paper is dedicated to Ed Spiegel. If it was not for the radiative time step problem, the Brandenburg & Spiegel (2006) paper would have been published by now! AB also acknowledges Fazeleh (Sepideh) Khajenabi for her work on the radiative time step problem while visiting Nordita in the spring of 2010. This research was supported in part by the National Science Foundation under the Astronomy and Astrophysics Grants Program (grant 1615100), and the University of Colorado through its support of the George Ellery Hale visiting faculty appointment. Simulations presented in this work have been performed with computing resources provided by the Swedish National Allocations Committee at the Center for Parallel Computers at the Royal Institute of Technology in Stockholm.

### References

- Balbus, S. A., & Hawley, J. F., “A powerful local shear instability in weakly magnetized disks. I. Linear analysis,” *Astrophys. J.* **376**, 214–222 (1991).
- Barekat, A., & Brandenburg, A., “Near-polytropic stellar simulations with a radiative surface,” *Astron. Astrophys.* **571**, A68 (2014).
- Bhat, P., & Brandenburg, A., “Hydraulic effects in a radiative atmosphere with ionization,” *Astron. Astrophys.* **587**, A90 (2016).
- Bingert, S., & Peter, H., “Intermittent heating in the solar corona employing a 3D MHD model,” *Astron. Astrophys.* **530**, A112 (2011).
- Bourdin, Ph.-A., Bingert, S., & Peter, H., “Observationally driven 3D magnetohydrodynamics model of the solar corona above an active region,” *Astron. Astrophys.* **555**, A123 (2013).
- Brandenburg, A., “Computational aspects of astrophysical MHD and turbulence,” In *Advances in nonlinear dynamos (The Fluid Mechanics of Astrophysics and Geophysics, Vol. 9)* (ed. A. Ferriz-Mas & M. Núñez), pp. 269–344. Taylor & Francis, London and New York (2003).
- Brandenburg A., “Stellar mixing length theory with entropy rain,” *Astrophys. J.* **832**, 6 (2016).
- Brandenburg, A., Nordlund, Å., Stein, R. F., & Torkelsson, U., “Dynamo generated turbulence and large scale magnetic fields in a Keplerian shear flow,” *Astrophys. J.* **446**, 741–754 (1995).
- Caunt, S. E., & Korpi, M. J., “A 3D MHD model of astrophysical flows: Algorithms, tests and parallelisation,” *Astron. Astrophys.* **369**, 706–728 (2001).
- Coleman, M. S. B., Blaes, O., Hirose, S., & Hauschildt, P. H., “Convection enhances magnetic turbulence in AM CVn accretion disks,” *Astrophys. J.* **857**, 52 (2018).
- Courant, R., Friedrichs, K., & Lewy, H., “Über die partiellen Differenzgleichungen der mathematischen Physik,” *Mathematische Annalen*, **100**, 32–74 (1928); Engl. Transl.: On the partial difference equations of mathematical physics, *IBM J. Res. Dev.*, **11**, 215–234 (1967).
- Deardorff, J. W., “The Counter-Gradient Heat Flux in the Lower Atmosphere and in the Laboratory,” *J. Atmosph. Sci.* **23**, 503–506 (1966).
- Deardorff, J. W., “Theoretical expression for the countergradient vertical heat flux,” *J. Geophys. Res.* **77**, 5900–5904 (1972).
- Edwards, J. M., “Two-dimensional radiative convection in the Eddington approximation,” *Month. Not. Roy. Astron. Soc.* **242**, 224–234 (1990).
- Frank, J., King, A. R., & Raine, D. J. *Accretion power in astrophysics*. Cambridge: Cambridge Univ. Press (1992).
- Gudiksen, B. V., & Nordlund, Å., “Bulk Heating and Slender Magnetic Loops in the Solar Corona,” *Astrophys. J.* **572**, L113–L116 (2002).
- Gudiksen, B. V. & Nordlund, Å., “An ab initio approach to solar coronal heating problem,” *Astrophys. J.* **618**, 1020–1030 (2005a).
- Gudiksen, B. V., & Nordlund, Å., “An ab initio approach to solar coronal loops,” *Astrophys. J.* **618**, 1031–1038 (2005b).
- Heinemann, T., Dobler, W., Nordlund, Å., & Brandenburg, A., “Radiative transfer in decomposed domains,” *Astron. Astrophys.* **448**, 731–737 (2006).
- Heinemann, T., Nordlund, Å., Scharmer, G. B., Spruit, H. C., “MHD simulations of penumbra fine structure,” *Astrophys. J.* **669**, 1390–1394 (2007).

- Hurlburt, N.E., Toomre, J., Massaguer, J.M., “Two-dimensional compressible convection extending over multiple scale heights,” *Astrophys. J.* **282**, 557–573 (1984).
- Kähler, H., “The local Vogt-Russell theorem,” *Astron. Astrophys.* **20**, 105–110 (1972).
- Käpylä, P. J., Rheinhardt, M., Brandenburg, A., Arlt, R., Käpylä, M. J., Lagg, A., Olsper, N., & Warnecke, J., “Extended subadiabatic layer in simulations of overshooting convection,” *Astrophys. J. Lett.* **845**, L23 (2017).
- Käpylä, P. J., Viviani, M., Käpylä, M. J., Brandenburg, A. & Spada, F., “Effects of a subadiabatic layer on convection and dynamos in spherical wedge simulations,” *Geophys. Astrophys. Fluid Dynam.*, arXiv:1803.05898 (2019).
- Kippenhahn, R., & Weigert, A. *Stellar structure and evolution*. Springer: Berlin (1990).
- Lasota, J.-P., “The disc instability model of dwarf novae and low-mass X-ray binary transients,” *New Astron. Rev.* **45**, 449–508 (2001).
- Mihalas, D. *Stellar Atmospheres*. W. H. Freeman: San Francisco (1978).
- Nordlund, Å., “Numerical simulations of the solar granulation I. Basic equations and methods,” *Astron. Astrophys.* **107**, 1–10 (1982).
- Nordlund, Å., Ramsey, J. P., Popovas, A., & Küffmeier, M., “DISPATCH: a numerical simulation framework for the exa-scale era - I. Fundamentals,” *Month. Not. Roy. Astron. Soc.* **477**, 624–638 (2018).
- Owocki, S. P., & Sundqvist, J. O., “Characterizing the turbulent porosity of stellar wind structure generated by the line-deshadowing instability,” *Month. Not. Roy. Astron. Soc.* **475**, 814–821 (2018).
- Prendergast, K. H., & Spiegel, E. A., “Photon Bubbles,” *Comm. Astrophys. Spa. Phys.* **5**, 43–50 (1973).
- Rüdiger, G. *Differential rotation and stellar convection: Sun and solar-type stars*. Gordon & Breach, New York (1989).
- Spiegel, E. A., “The smoothing of temperature fluctuations by radiative transfer,” *Astrophys. J.* **126**, 202–207 (1957).
- Spiegel, E. A., “Photoconvection,” In *Problems of stellar convection* (ed. Proceedings of the Thirty-eighth Colloquium, Nice, France, August 16-20, 1976), pp. 267–283. Berlin and New York: Springer-Verlag (1977).
- Spiegel, E. A., “Phenomenological photofluidynamics,” *EAS Publ. Ser.* **21**, 127–145 (2006).
- Spiegel, E. A., & Tao, L., “Photofluid instabilities of hot stellar envelopes,” *Phys. Rev.* **311**, 163–176 (1999).
- Stein, R. F., & Nordlund, Å., “Topology of convection beneath the solar surface,” *Astrophys. J. Lett.* **342**, L95–L98 (1989).
- Stein, R. F., & Nordlund, Å., “Simulations of solar granulation: I. General properties,” *Astrophys. J.* **499**, 914–933 (1998).
- Stix, M. *The Sun: An introduction*. Springer-Verlag, Berlin (2002).
- Stone, J. M., & Norman, M., “ZEUS-2D: A radiation magnetohydrodynamics code for astrophysical flows in two space dimensions: I. The hydrodynamic algorithms and tests,” *Astrophys. J.* **80**, 753–790 (1992a)
- Stone, J. M., & Norman, M., “ZEUS-2D: A radiation magnetohydrodynamics code for astrophysical flows in two space dimensions: II. The magnetohydrodynamic algorithms and tests,” *Astrophys. J.* **80**, 791–818 (1992b)
- Stone, J. M., Mihalas, D., & Norman, M., “ZEUS-2D: A radiation magnetohydrodynamics code for astrophysical flows in two space dimensions: III. The radiation hydrodynamic algorithms and tests,” *Astrophys. J.* **80**, 791–818 (1992)
- Sundqvist, J. O., Owocki, S. P., & Puls, J., “2D wind clumping in hot, massive stars from hydrodynamical line-driven instability simulations using a pseudo-planar approach,” *Astron. Astrophys.* **611**, A17 (2018).
- Trampedach, R., Asplund, M., Collet, R., Nordlund, Å., Stein, R. F., “A Grid of Three-dimensional Stellar Atmosphere Models of Solar Metallicity. I. General Properties, Granulation, and Atmospheric Expansion,” *Astrophys. J.* **769**, 18 (2013).
- Unno, W., & Spiegel, E. A., “The Eddington approximation in the radiative heat equation,” *Publ. Astron. Soc. Jap.* **18**, 85–95 (1966).
- Vitense, E., “Die Wasserstoffkonvektionszone der Sonne,” *Z. Astrophys.* **32**, 135–164 (1953).
- von Neumann, J., & Richtmyer, R. D., “A method for the numerical calculation of hydrodynamic shocks,” *J. Appl. Phys.* **21**, 232–237 (1950).
- Williamson, J. H., “Low-storage Runge-Kutta schemes,” *J. Comp. Phys.* **35**, 48–56 (1980).

## Appendix A: Improved outer radiative boundary condition

In section 3.4, we stated that the assumption of zero incoming intensity is not accurate when we want to reproduce the analytic solution for an infinitely extended layer, where the gas beyond the simulated boundary does contribute to producing incoming radiation. To take this into account, we assume that  $F_{\text{rad}}$  is known and that the system is in radiative equilibrium. In

that case, and with just two rays,  $I_{\pm} = I(\mathbf{x}, t, \pm\hat{\mathbf{z}})$ , we have

$$S = J = (I_+ + I_-)/2, \quad F_{\text{rad}}/4\pi = (I_+ - I_-)/2, \quad (\text{A.1})$$

so  $I_{\pm} = (S \pm F_{\text{rad}}/4\pi)/2$ . In the PENCIL CODE, this boundary condition is invoked by stating the symbolic name `bc_rad='p', 'p', 'S+F:S-F'`.

### Appendix B: Relation between pressure and density scale heights

As stated in section 4.3,  $H_p = H_\rho$  for an isothermal stratification. For an isentropic stratification, we have  $\gamma H_p = H_\rho$ . The general relation is given by

$$\nabla - \nabla_{\text{ad}} = \frac{d(s/c_p)}{d \ln p} = \frac{1}{\gamma} - \frac{d \ln \rho}{d \ln p} = \frac{1}{\gamma} - \frac{H_p}{H_\rho}. \quad (\text{B.1})$$

Thus, since  $\nabla_{\text{ad}} = 1 - 1/\gamma$ , we have

$$H_p/H_\rho = \nabla - 1, \quad (\text{B.2})$$

which is independent of  $\gamma$ . In the absence of convection, and for simple power law opacities given by equation (24) with single exponents  $a$  and  $b$ , the double-logarithmic temperature gradient  $\nabla = 1/(1 + n)$  depends on the polytropic index  $n = (3 - b)/(1 + a)$  (Barekat & Brandenburg 2014). In table B1, some examples are listed.

Table B1. Examples of  $H_p/H_\rho$  for different types of stratification.

	$\gamma$	$a$	$b$	$n$	$\nabla$	$H_p/H_\rho$
isentropic	5/3	1	0	1.5	0.4	0.6
elect scattering	5/3	0	0	3	0.25	0.75
Kramers opacity	5/3	1	-3.5	3.25	0.235	0.765
	5/3	0	arbitr	$\infty$	0	1
isothermal	1	0	arbitr	$\infty$	0	1 (indep of $\gamma$ )